

Hyperuniformity on Mars: Pebbles scattered on sand

Zheng Zhu¹, Bernard Hallet², András A. Sipos^{3,4}, Gábor Domokos^{3,4}, and Quan-Xing Liu^{5*}

AFFILIATIONS

1. Research Center of Global Change and Complex Ecosystems, School of Ecological and Environmental Sciences, East China Normal University, 200241 Shanghai, China.
2. Department of Earth and Space Sciences and Quaternary Research Center, University of Washington, Seattle, WA 98195, USA.
3. Department of Morphology and Geometric Modeling, Budapest University of Technology and Economics, Műegyetem rkp 3, H-1111 Budapest, Hungary.
4. HUN-REN-BME Morphodynamics Research Group, Budapest University of Technology and Economics, Műegyetem rkp 3, H-1111 Budapest, Hungary.
5. School of Mathematical Sciences, Shanghai Jiao Tong University, Shanghai 200240, China.

*CORRESPONDING AUTHORS. Email: qx.liu@sjtu.edu.cn;

Tel Phone: 086 13661642723

Abstract (197 words)

In Gale Crater near Mars' equator, dunes and ripples of sand stand out from the general orderless, rocky terrain. In addition, images from Curiosity, the Mars Science Laboratory rover, reveal more subtle orderly forms: widespread, meter-scale domains of evenly spaced, pebble-size rocks (termed clasts) on wind-blown sand in scattered locations. Here, we examine quantitatively several clast domains on both Mars and Earth, and compare their geometry with that of random points. The clast distributions are more orderly than expected by chance; they differ significantly from those associated with uniform (Poisson) random processes. Moreover, they are hyperuniform, a self-organized state recently recognized in diverse active materials and biological systems but that appears novel for planetary surfaces. These patches are often surrounded by recent wind-borne ripples, suggesting an interplay between sand transport, ripple activity and clasts. Using numerical simulations, we show that clast displacements induced by gravity, combined with the evolution of the sand surface caused by aeolian sand transport and ripple migration, can produce realistic hyperuniform and random clast distributions, as well as distinct clast alignments. Our findings highlight the existence of easily overlooked disordered hyperuniform states on ground surfaces, suggesting novel self-organized states beyond distinct geometric patterns.

Keywords: Patterned ground, disordered hyperuniformity, self-organization

Main text:

The natural world around us exhibits distinct patterns at all scales in diverse systems, from cellular structures to organs (1, 2), and from ecosystems to landscapes (3-5). Since the seminal work of Alan Turing on pattern formation in biological systems (6), a large body of experimental evidence and theoretical work has shown that these patterns are largely due to scale-dependent feedbacks (7, 8). These self-organized patterns in nature are intriguing, as they suggest that a multitude of particles, whether animate or not, can collectively act in an organized manner in response to local interactions (9). Theoretical models, aided by measurements, have shed light on the underlying processes and mechanisms by enabling diagnostic comparisons of observed and simulated patterns (5, 10, 11). For instance, the models elucidate how self-organized patterns in biological systems can affect mesoscale stability and potential energy, thereby improving resilience to perturbation and environmental change (12-14). Thus, self-organized patterns are intrinsically interesting, and they invite focused attention on the underlying processes that has yielded considerable insight.

Distinct self-organized landforms and bedforms -- sand dunes and ripples -- and geometric patterns of rock fragments on planetary surfaces -- stripes, circles, and labyrinths -- are well-recognized (e.g. (11, 15-18)). On Earth, such patterns are generally known as patterned ground, best developed where environmental fluctuations cause exchange of moisture and energy with the atmosphere and freeze-thaw cycles in the subsurface (19, 20). The self-organization manifests interactions and feedbacks involving transport of heat and moisture, as well as phase changes and local strain fields in granular material. These repeated freeze-thaw cycles drive aggregation and segregation of coarse clasts from random states (4, 21). In contrast with aeolian forms (22, 23) and patterned ground (4, 5, 21), which have been studied extensively from a self-organization perspective, uniform clast dispersions have received little close attention.

At the Spirit landing site on Mars, the uniform dispersion of clasts, too large to be entrained by wind, was one of the most enigmatic discoveries about the planet from the early rovers (24, 25). More uniformly spaced distributions were found in all areas than expected for random distributions, with one exception: especially coarse and recent impact-ejecta deposits (24). These data were utilized, along with results from wind-tunnel experiments and numerical simulations, in the pioneering, comprehensive study of clast distributions (24). On Earth, evenly spaced clasts on sand surfaces have been observed and puzzled over for decades, extending back at least to Bagnold's (26) early descriptions of the tendency of pebbles on sand to disperse "*to the most uniform distribution possible*". Such distributions are not limited to active aeolian surfaces; for

instance, Walker and Harms reported examples from the ancient stratigraphic record (27, figure 16).

Here, we document the spatial distributions of clasts on sand and probe their geometry in detail using MastCam images acquired from the Mars Science Laboratory (MSL) rover, Curiosity (28) in Gale Crater, Mars. For comparison, we also analyze clast images from the Gobi Desert on Earth. For several sand sites interspersed in rocky terrain where surface clasts appeared uniformly dispersed, we examine quantitatively the clast distribution in meter-scale sand domains (Fig. 1 and Figs. S1 to S3). These domains are distinct from aeolian bedforms that commonly form extensive fields of well sorted sand with coarser grains locally covering bedform crests (29). We leverage the pioneering studies of clast distributions (24-26), and augment them in several ways by 1) using recent and higher resolution Mars images (down to 150 micron per pixel) from Curiosity to better document the characteristics of clast distributions on sandy surfaces within Gale Crater and, for comparison, Earth images from the Gobi Desert, 2) characterizing the clast distributions rigorously, 3) interpreting them in the rich, contemporary context of hyperuniformity as introduced in the following paragraph, and 4) developing an augmented model of eolian redistribution of clasts on sand that includes the significant role of migrating ripples and leads to three distinct patterns similar to those seen in nature.

Much insight into clast distributions can be gained from recent advances in studies of active matter across many fields that include the recognition of an important type of spatial distribution, known as hyperuniform (30-33). Hyperuniform distributions in mixed-component, multi-particle systems are those with unusually low fluctuations in component density at large scales, when compared to disordered systems such as mixed ideal gases or typical liquids. Some of these systems, known as disordered hyperuniform systems, are statistically isotropic, and exhibit anomalous small long-wavelength (i.e., large scale) density fluctuations, similar to crystals (30, 32). Hyperuniform systems are gaining increasing attention across the physical (34-38) and biological sciences (39-42), partly because of the many optimal properties of such systems such as the lack of diffraction in photonic materials (43) and system free energy minima in two-phase heterogeneous materials (44). For instance, marine algal cells can self-organize into disordered hyperuniform distributions that maximize nutrient uptake at air-liquid interfaces through repulsive interactions (40, 45). The connections of hyperuniform states of matter to many different areas of fundamental science are profound and yet their implications for the rich array of patterns in landscapes have not been explored.

Hyperuniform distributions of clasts

We first compare spatial distributions of observed clasts and those of random points. The point set representing the observed clasts is compared with points obtained from a homogeneous Poisson point process (Fig. 2a and 2b). Two-sided Kolmogorov-Smirnov tests reveal a significant difference between them ($p < 0.001$, $Z = 0.224$). There is no overlap of statistical parameters using either edges lengths or areas of the Delaunay triangles. Several sites yielded comparable results with statistically significant difference between observed clasts and random points. Figures S4 and S5 show six additional pebble distributions on Mars and Earth and their random counterparts. In addition, their standard deviations and R values, the spacing measure defined by Ward et al. (25) are listed in Tables S5 and S6. R is calculated by dividing the average nearest neighbor distance (r_A) by the expected average nearest neighbor distance (r_E) of a random distribution. Hence, although the Poisson process is the best understood random process that can produce spatially uniform distributions, the observed pebbles on Mars and on Earth are still more spatially uniform than can result from chance; most likely they are self-organized.

Second, we investigate the distribution of clasts in greater detail utilizing static structure factors, S , which are widely used in diverse disciplines ranging from condensed matter physics to ecology (see Materials and Methods for details). The clasts show a scaling behavior typical of hyperuniformity: S increases with the wavenumber ($2\pi/\text{mean clast spacing}$), k , as $S(k) \sim k^{0.4}$ in the small k regions, and then fluctuates around ~ 1.0 , which is typical of random points in the large k regions (Fig. 3a). We also compute areal density fluctuations of the clasts (Fig. 3b and Fig. S6). Over large areas, represented by large length scales, ℓ , density fluctuations follow the scaling law determined by the central limit theorem (large numbers of independent and identically distributed random variables tend to follow a normal distribution as the sample size increases). Density fluctuations first decay nonlinearly (exponent, $\alpha \sim -2.4$) with increasing ℓ up to a value above which they stabilize, and then approach randomness with the exponent of $\alpha = -2.0$ (Fig. 3b). We note that in two dimensions, $\alpha = -2.0$ for random patterns, $-3.0 < \alpha < -2.0$ for hyperuniform distributions, and $\alpha \sim -3.0$ for crystals because of the standard surface-area scaling. We calculate the pair-correlation function as well. The peak represents the center-to-center neighbor distance, ~ 7 mm, at which clasts tend to be found most frequently relative to that expected for random distribution (Fig. 3c).

For vanishing k , the deviation from hyperuniformity with decreasing k of the structure factor $S(k)$, suggests that the clasts never self-organize into full hyperuniformity through the entire system. Nevertheless, hyperuniform regions can extend as far as ~ 10

clast diameters. For instance, the hyperuniform scale for sol 3303 with mean clast diameters of 3 mm can reach 30 mm ($k \sim 0.03 \text{ mm}^{-1}$ in Fig. 3a). Very similar results were found on Earth in the Gobi desert (Fig. 3, d to f). The static structure factors and density fluctuations for the data all show the consistent scaling hallmark of disordered hyperuniformity (30, 32, 36, 40). We stress that according to the value of the exponent at small k , within the hyperuniform region in the system, this hyperuniformity is the weakest form reported in the literature (e.g. ref. (46), section 5); it is referred to as class III disordered hyperuniformity.

Numerical model of wind-driven clast distributions

We used numerical simulations to shed light on the physical mechanisms that underlie the hyperuniformity by leveraging previous numerical studies and observations of wind effects on sand surfaces (22, 24, 29). We developed a cellular automata (particle-based) model of clast displacement, sand transport, ripple development, and local erosion-deposition around clasts. Clast motion is expected to respond to the sand surface evolution because the local surface slope changes significantly as ripples grow and migrate, and as sand erosion (and deposition) is enhanced upwind (and downwind) of each clast. The numerical model, which has much in common with a previous model of clast movement on flat sand (24), is useful in elucidating the evolution of clast distributions on sand (movie S1). It also readily yields disordered hyperuniform clast distributions very similar to those found on sand surfaces at various sandy sites both in Gale crater and the Gobi Desert.

The simulated clast distributions are quantitatively consistent with those imaged on Mars. They show similar scaling for both the structure factors (Figs. 3a and 4b) and density fluctuations (Figs. 3b and 4b). Specifically, the exponent of the static structure factor gradually decreases with time (number of time steps) and then stabilizes near a value of 0.3 (Fig. S7). Furthermore, the density fluctuations of the imaged (both Gale and Gobi) and modeled clasts are consistent with one another; they both yield structure factor exponents that converge to a value around 0.6 (Figs. 3d and 4c), which corresponds to the exponent of about -2.6 for the density fluctuations (Figs. 3e and 4d). The spacing between adjacent clasts tends to increase with ripple wavelength in both the data and in the simulations, reflecting their shared dependence on the local wind-velocity and saltation lengths (Figs. S8 and S9). For the simulations in Fig. 4, the length and width of the modeled sand surface were set to 1024, a value nondimensionalized by the mean sand diameter (2 mm for clast in Gale, see Fig. S2; 20 mm for clast in Gobi). Results from two simulations are presented: the first with 400 clasts initially distributed randomly in a square, covering ~53% of its area (Fig. 4a and 4b), and the second with 2000 clasts initially distributed randomly in a rectangle, covering ~36% of

its area (Fig. 4c and 4d and movie S2). Simulation results are very consistent with the observed data for the hyperuniform distribution; they all yield a local disordered hyperuniform range (Fig. S10), which can extend as far as ~ 10 clast radii.

To explore potential self-organizing aeolian processes, two types of level sand surfaces were considered, one with ripple migration and growth (Fig. S11 and movie S1), and the other without ripples (34). Models with dynamic ripples lead to disordered hyperuniform clast distributions more readily than those without ripples. The ripples make clasts particularly susceptible to lateral diffusion as clasts tend to roll stochastically into windward troughs (Figs. S12 and S13). Our numerical simulations, show how disordered hyperuniformity develops quickly at local scales and more slowly as the scale increases (Fig. 4 and S7). The progressive self-organization is slow, hence hyperuniformity is only partially achieved at the scale of the entire system. Note that for all numerical simulations presented here, the clast diameter was 11 times that of the sand particles. Surprisingly, this numerical choice, which was arrived at empirically, is consistent with early field observations of the dispersion of pebbles on a sand surface by Bagnold (26); he wrote that for clasts to disperse evenly on sand “the ratio of the two peak diameters [of clasts and sand] should exceed 10 to 1.”

A phase diagram for clast distributions and disordered hyperuniformity

According to our numerical model two physical parameters (saltation distance and diameter ratio), represented by the density fluctuations exponent, α , control the transition between three types of clast distributions readily visualized in a phase diagram (Fig. 5a): a random state (blue regime), hyperuniform distributions (green regime) and distributions featuring clast alignments (purple regime). The hyperuniformity and clast alignments form spontaneously starting from an initial random dispersion.

The range of the density fluctuation exponent (α) serves as an indicator for identifying the obscured arrangement of clast distribution, as was shown in Fig. 4. The emergence of disordered hyperuniform distributions is governed by thresholds in saltation distance and clast-to-sand diameter ratio. For example, the diameter ratio must be at least 10:1 to generate hyperuniformity under the lowest wind speed condition (Fig. 5a). For comparison, Fig. 5b to d show simulated clast patterns for different values of α , and Fig. 5e to g show images of actual clast patterns from images on Mars. The diversity of clast distributions remains robust across various physical environments, regardless of clast numbers and initial states. Our model based findings provide a unifying framework for understanding bimodal surface textures of aeolian bedforms on Mars and Earth.

Discussion

Over the past two decades, significant research has focused on disordered structures, contrasting with ordered crystals (30, 39, 47). Until very recently, only two types of hyperuniform distributions have been recognized in experimental and numerical studies: ones governed by long-range weak interplay of hydrodynamic interactions and others by critical absorbing phase transitions, as well as local interactions and periodic forces (48). Here, we introduce a third type, a natural landscape feature on Mars and Earth governed by the interplay of aerodynamic forces and local relief. These uniform clast domains on sand exemplify a broad class of physical systems with self-organized, hyperuniform distributions extending over areas much larger than the individual element. This subtle spatial self-organized state may reflect novel functions and processes, prompting a reassessment of physical mechanisms underlying various irregular self-organized patterns.

Our simulations shed light on how clasts interact with their neighbors via their collective effects on the near-surface wind field and resulting patterns of sand erosion and deposition (24). Moving ripples also alter clast displacements, locally deviating and accelerating the slow, generally upwind clast migration. Additionally, the ripples reported herein, from both the Mars images and simulations are consistently centimeter scale. This suggests that they are impact ripples, where grains synchronize with the topography, rather than aerodynamic ripples, which involve a phase shift between turbulent flow and topography (49). Our results suggest that disordered hyperuniformity is a novel stable state for dispersed clasts on sand between random distributions and alignments; it requires optimal wind speeds.

Our simulations represent a modest first step in understanding the complex development of actual aeolian textures and clast dispersions. We have implicitly assumed that the clast distributions are currently active and produced by contemporary sand processes and steady wind directions, but stress that more complex scenarios are to be expected, in general. Clast distributions seen in the rock record necessarily involve burial and exhumation and, hence a history involving temporal variations wind strength, orientation, and sediment flux.

More generally, sand transport and related eolian process commonly generate clear spatial variability in the texture of bedform surfaces, including concentrations of large grains at the crest of large ripples, where they can form a continuous cover with adjacent grains in contact with another; they can also stack to form the crestral region of larger bedforms (23, 29, 49). These clast concentrations contrast with the domains of dispersed clasts examined herein that very seldom contact one another and that are on sand interspersed in rocky terrain near scattered sources of rock fragments mechanically

weathered from nearby rock surfaces.

Clasts in rocky terrain on Mars also form intriguing ground patterns in widely scattered sites on dry regolith surfaces near the equator in Gale Crater (50) and Gusev Crater (25). For instance, clasts are well-sorted and organized spatially according to size, the larger ones concentrating along ridges. These ground patterns are hypothesized to arise from small, inferred cyclic expansion and contraction of the bedrock and regolith driven by environmental fluctuations (15). However, the relative contributions to ground pattern formation of aeolian processes and granular processes driven by cyclic volumetric variations in the regolith are poorly known, and are likely to vary considerably according to local near-surface wind speeds and direction, as well as regolith properties and environmental forcings.

Our numerical simulations suggest that ripples and hyperuniform clast distributions both arise from stochastic sand grain impacts and subsequent grain motion over the uneven sand surface. The migration of ripples and clasts can lead to clast alignments paralleling ripple crests (see [movies S1](#) and [Fig. S13](#)). The frequency of transverse clast displacements significantly increases when ripples emerge (see [Fig. S12](#)) while the hyperuniformity emerges. This passive movement mechanism is also supported by independent particle simulations in quite different systems that share similar underlying principles. For instance, long-range interactions are not required for the formation of hyperuniform patterns (44), and the migration of ripples forced by stochastic forces on clasts functions much as in periodically-driven emulsions (48). Furthermore, the important finding is that both the alignment and hyperuniformity of self-organized distributions are elucidated through numerical simulations and phase diagrams.

In summary, herein we draw attention to local domains of uniformly dispersed clast on sand, a form of self-organization on Mars and Earth that may be widespread, but only rarely recognized because the uniform domains are considerably less noticeable than sand dunes and other bedforms, and distinct geometric ground patterns (50). Moreover, the meter-scale clast domains on Mars are too small to be detected from orbit. Borrowing from fundamental fields --physics, material science and biology-- we introduce concepts and quantitative descriptors (structure factor and pair-correlation function that are novel in the field of aeolian processes) of the spatial distribution of clasts on sand surfaces on Gale Crater, Mars. These may also prove useful in studies of diverse clast distributions on various ground surfaces -- sediment and regolith surfaces, erosional lags, clast armors and (desert) pavements -- on earth and other planets. These descriptors also facilitate quantitative comparison between empirical data and results of numerical models used to probe formative mechanisms involving wind and other effects in granular systems. Moreover, we present our results leveraging rich insights into manifestations of hyperuniformity gained recently in diverse disciplines.

We note that although our study initially targeted pebble distributions on Mars, it led to unprecedented, quantitative characterization of pebble distributions on Earth, which is an understudied dimension of dust emission, a significant contemporary societal issue (51). It also bears on the interpretation of dust (loess) stratigraphic records that are valuable resources for understanding atmospheric and aeolian processes. These records can offer insight into past climate changes, environmental factors influencing dust production, and the transport of dust in planet's atmosphere (52). Lastly, inspired by many studies that have revealed forms of optimality in diverse other hyperuniform systems, we suggest a hypothesis suitable for future testing: for a given concentration of clasts on sand, the spatial distribution of clasts that armors the sand most effectively is hyper-uniform. This may help understand both the common occurrence of hyperuniform clast patches, and the transient nature of less uniform patches. This spatiotemporal dimension of pattern formation merits close attention in future studies of ecosystems (12, 53, 54) and in biogeomorphology (55).

Reference

1. F. J. Nedelec, T. Surrey, A. C. Maggs, S. Leibler, Self-organization of microtubules and motors. *Nature* **389**, 305-308 (1997).
2. M. C. Wigbers *et al.*, A hierarchy of protein patterns robustly decodes cell shape information. *Nature Physics* **17**, 578-584 (2021).
3. M. Lämmel *et al.*, Aeolian sand sorting and megaripple formation. *Nature Physics* **14**, 759-765 (2018).
4. A. Li *et al.*, Ice needles weave patterns of stones in freezing landscapes. *Proc Natl Acad Sci USA* **118**, e2110670118 (2021).
5. M. Kessler, B. Werner, Self-organization of sorted patterned ground. *Science* **299**, 380-383 (2003).
6. A. M. Turing, The chemical basis of morphogenesis. *Phil Tran Roy Soc Lond Series B* **237**, 37-72 (1952).
7. J. van de Koppel *et al.*, Experimental evidence for spatial self-organization and its emergent effects in mussel bed ecosystems. *Science* **322**, 739-742 (2008).
8. H. Meinhardt, *The algorithmic beauty of sea shells* (Springer-Verlag, Berlin, Heidelberg, New York, 2009), 10.1007/978-3-540-92142-4, pp. 269.
9. S. Camazine, *Self-organization in biological systems*, Princeton studies in complexity (Princeton University Press, Princeton, N.J., 2001), pp. viii, 538 p.
10. I. Rodriguez-Iturbe, A. Rinaldo, *Fractal river basins: Chance and self-organization* (Cambridge University Press, Cambridge, U.K.; New York, 1997), pp. xvi, 547 p.
11. W. Rapin *et al.*, Sustained wet-dry cycling on early Mars. *Nature* **620**, 299-302 (2023).

12. W. S. Hu *et al.*, Disordered hyperuniformity signals functioning and resilience of self-organized vegetation patterns. *arXiv [Preprint]* <https://doi.org/10.48550/arXiv.2311.07624> (2023).
13. C. Schwarz *et al.*, Self-organization of a biogeomorphic landscape controlled by plant life-history traits. *Nature Geoscience* **11**, 672-677 (2018).
14. K. Siteur *et al.*, Phase-separation physics underlies new theory for the resilience of patchy ecosystems. *Proc Natl Acad Sci USA* **120**, e2202683120 (2023).
15. B. Hallet *et al.*, Active ground patterns near Mars' equator in the Glen Torridon region of Gale Crater. *Journal of Geophysical Research: Planets* **127**, e2021JE007126 (2022).
16. T. Adachi *et al.*, Forced into an ecological corner: Round-the-clock deep foraging on small prey by elephant seals. *Sci Adv* **7** (2021).
17. N. T. Bridges, B. L. Ehlmann, The Mars Science Laboratory (MSL) Bagnold Dunes Campaign, Phase I: Overview and introduction to the special issue. *J Geophys Res Planets* **123**, 3-19 (2018).
18. M. C. Malin *et al.*, Early views of the Martian surface from the Mars orbiter camera of Mars global surveyor. *Science* **279**, 1681-1685 (1998).
19. A. E. Corte, Particle sorting by repeated freezing and thawing. *Science* **142**, 499-501 (1963).
20. B. Hallet, Stone circles: form and soil kinematics. *Philos Trans A Math Phys Eng Sci* **371**, 20120357 (2013).
21. B. T. Werner, B. Hallet, Numerical simulation of self-organized stone stripes. *Nature* **361**, 142-145 (1993).
22. B. T. Werner, Eolian dunes: Computer simulations and attractor interpretation. *Geology* **23**, 1107-1110 (1995).
23. K. Tholen, T. Pahtz, H. Yizhaq, I. Katra, K. Kroy, Megaripple mechanics: Bimodal transport ingrained in bimodal sands. *Nat Commun* **13**, 162 (2022).
24. J. D. Pelletier, A. L. Leier, J. R. Steidtmann, Wind-driven reorganization of coarse clasts on the surface of Mars. *Geology* **37**, 55-58 (2009).
25. J. G. Ward, R. E. Arvidson, M. Golombek, The size-frequency and areal distribution of rock clasts at the Spirit landing site, Gusev Crater, Mars. *Geophys Res Lett* **32**, L11203 (2005).
26. R. A. Bagnold, *The physics of blown sand and desert dunes* (Methuen, London, 1941), 10.1007/978-94-009-5682-7, pp. 265.
27. T. R. Walker, J. C. Harms, Eolian origin of flagstone beds, Lyons Sandstone (Permian), Type Area, Boulder County, Colorado. *The mountain Geologist* **9**, 279-288 (1972).
28. M. C. Malin *et al.*, The Mars Science Laboratory (MSL) Mast cameras and Descent imager: Investigation and instrument descriptions. *Earth Space Sci* **4**, 506-539 (2017).
29. R. Sullivan *et al.*, The Aeolian Environment in Glen Torridon, Gale Crater, Mars. *J Geophys Res Planets* **127**, e2021JE007174 (2022).
30. S. Torquato, Hyperuniform states of matter. *Physics Reports* **745**, 1-95 (2018).

31. D. Hexner, P. M. Chaikin, D. Levine, Enhanced hyperuniformity from random reorganization. *Proc Natl Acad Sci USA* **114**, 4294-4299 (2017).
32. S. Torquato, F. H. Stillinger, Local density fluctuations, hyperuniformity, and order metrics. *Phys Rev E* **68**, 041113 (2003).
33. A. Donev, F. H. Stillinger, S. Torquato, Unexpected density fluctuations in jammed disordered sphere packings. *Phys Rev Lett* **95**, 090604 (2005).
34. Q. L. Lei, M. P. Ciamarra, R. Ni, Nonequilibrium strongly hyperuniform fluids of circle active particles with large local density fluctuations. *Sci Adv* **5**, eaau7423 (2019).
35. S. Torquato, G. Zhang, F. H. Stillinger, Ensemble theory for stealthy hyperuniform disordered ground states. *Phys Rev X* **5**, 021020 (2015).
36. D. Hexner, D. Levine, Hyperuniformity of critical absorbing states. *Phys Rev Lett* **114**, 110602 (2015).
37. A. Chremos, J. F. Douglas, Hidden hyperuniformity in soft polymeric materials. *Phys Rev Lett* **121**, 258002 (2018).
38. R. Xie *et al.*, Hyperuniformity in amorphous silicon based on the measurement of the infinite-wavelength limit of the structure factor. *Proc Natl Acad Sci USA* **110**, 13250-13254 (2013).
39. S. Torquato, Swimming in circles can lead to exotic hyperuniform states of active living matter. *Proc Natl Acad Sci USA* **118**, e2107276118 (2021).
40. M. Huang, W. Hu, S. Yang, Q. X. Liu, H. P. Zhang, Circular swimming motility and disordered hyperuniform state in an algae system. *Proc Natl Acad Sci USA* **118** (2021).
41. Y. Jiao *et al.*, Avian photoreceptor patterns represent a disordered hyperuniform solution to a multiscale packing problem. *Phys Rev E* **89**, 022721 (2014).
42. D. K. Lubensky, M. W. Pennington, B. I. Shraiman, N. E. Baker, A dynamical model of ommatidial crystal formation. *Proc Natl Acad Sci USA* **108**, 11145-11150 (2011).
43. W. Man *et al.*, Isotropic band gaps and freeform waveguides observed in hyperuniform disordered photonic solids. *Proc Natl Acad Sci USA* **110**, 15886-15891 (2013).
44. S. Torquato, Disordered hyperuniform heterogeneous materials. *J Phys Condens Matter* **28**, 414012 (2016).
45. Z. Zhu, Q. X. Liu, Enhanced transport of nutrients powered by microscale flows of the self-spinning dinoflagellate *Symbiodinium* sp. *J Exp Biol* **222** (2019).
46. S. Torquato, Hyperuniform states of matter. *Phys Rep* **745**, 1-95 (2018).
47. M. Florescu, S. Torquato, P. J. Steinhardt, Designer disordered materials with large, complete photonic band gaps. *Proc Natl Acad Sci USA* **106**, 20658-20663 (2009).
48. J. H. Weijs, R. Jeanneret, R. Dreyfus, D. Bartolo, Emergent hyperuniformity in periodically driven emulsions. *Phys Rev Lett* **115**, 108301 (2015).

49. H. Yizhaq *et al.*, Coevolving aerodynamic and impact ripples on Earth. *Nature Geoscience* **17**, 66-72 (2024).
50. B. Hallet *et al.*, Active ground patterns near Mars' equator in the Glen Torridon region of Gale Crater. *J Geophys Res Planets* **127**, e2021JE007126 (2022).
51. N. Meijer *et al.*, Identifying eolian dust in the geological record. *Earth-Sci Rev* **211** (2020).
52. Z. Zhang, A. Bird, C. Zhang, Z. Dong, Not all gravel deserts in northern China are sources of regionally deposited dust. *Atmos Environ* **273**, 118984 (2022).
53. S. Torquato, Self-organized disordered vegetation patterns with hidden order in arid ecosystems. *Proc Natl Acad Sci USA* **120**, e2316879120 (2023).
54. Z. Ge, The hidden order of Turing patterns in arid and semi - arid vegetation ecosystems. *Proc Natl Acad Sci USA* **120**, e2306514120 (2023).
55. E. D. Lee, C. P. Kempes, G. B. West, Growth, death, and resource competition in sessile organisms. *Proc Natl Acad Sci USA* **118** (2021).
56. N. Otsu, A threshold selection method from gray-level histograms. *IEEE Trans Syst Man Cybern* **9**, 62-66 (1979).
57. C. Forbes, M. Evans, N. Hastings, B. Peacock, *Statistical Distributions. Fourth Edition* (John Wiley & Sons, Ltd, Hoboken, 2011).
58. J. King, W. G. Nickling, J. A. Gillies, Representation of vegetation and other nonerodible elements in aeolian shear stress partitioning models for predicting transport threshold. *J Geophys Res Earth Surf* **110**, F04015 (2005).
59. R. L. Miller, R. J. Byrne, The angle of repose for a single grain on a fixed rough bed. *Sedimentology* **6**, 303-314 (1966).
60. T. Wiegand, K. A. Moloney, *Handbook of spatial point-pattern analysis in ecology* (Taylor & Francis, Boca Raton, 2013), pp. 538.

Data availability

All analyzed data are available in the manuscript or supplementary materials. Further raw data are available at <https://mars.nasa.gov/msl/home/>. The data and their derivatives have been transferred to a figshare repository (<https://figshare.com/s/7d19ea1a53de94a4caa2>).

Code availability

All analysis and code data underlying this work are available from GitHub (<https://github.com/liuqx315/Clasts-Pattern-Mars/>) and figshare repository (<https://figshare.com/s/7d19ea1a53de94a4caa2>).

Author contributions

Z.Z. contributed to the analysis, modelling, and performed the simulations. B.H. and Q.X.L. conceptualization, data collection. A.A.S. and G.D. contributed to statistical

analysis, commented on the paper. Z.Z., B.H. and Q.X.L. contributed to interpretation of the results and writing of the manuscript.

Competing interests

The authors declare no competing interests.

Acknowledgements

We are grateful for NASA's support of the Mars Science Laboratory (MSL) mission and for the efforts of the large team of talented and dedicated scientists and engineers who made this work possible. We thank, in particular, T. Kubacki for his astute observations and his Malin Space Science Systems (MSSS) colleagues for their critical role in acquiring the images. MSSS kindly provided the image mosaic used in Fig. 1a. The authors also appreciate insightful discussions with H. P. Zhang, B. Werner, R. Sletten, R. Sullivan, and M. Malin that benefitted this paper. We thank G. C. Cheng and J. Chen for their assistances in taking the drone images and collecting the field data. Funding was provided by the National Science Foundation of China through award No. 32071609 (Q.X.L.), by the NKFIH Grant 134199 and the TKP2021-BME-NVA-470 02 program (G.D. and A.A.S.). B.H. gratefully acknowledges sustained funding through the MSL mission from a NASA grant awarded to MSSS.

Figures and captions

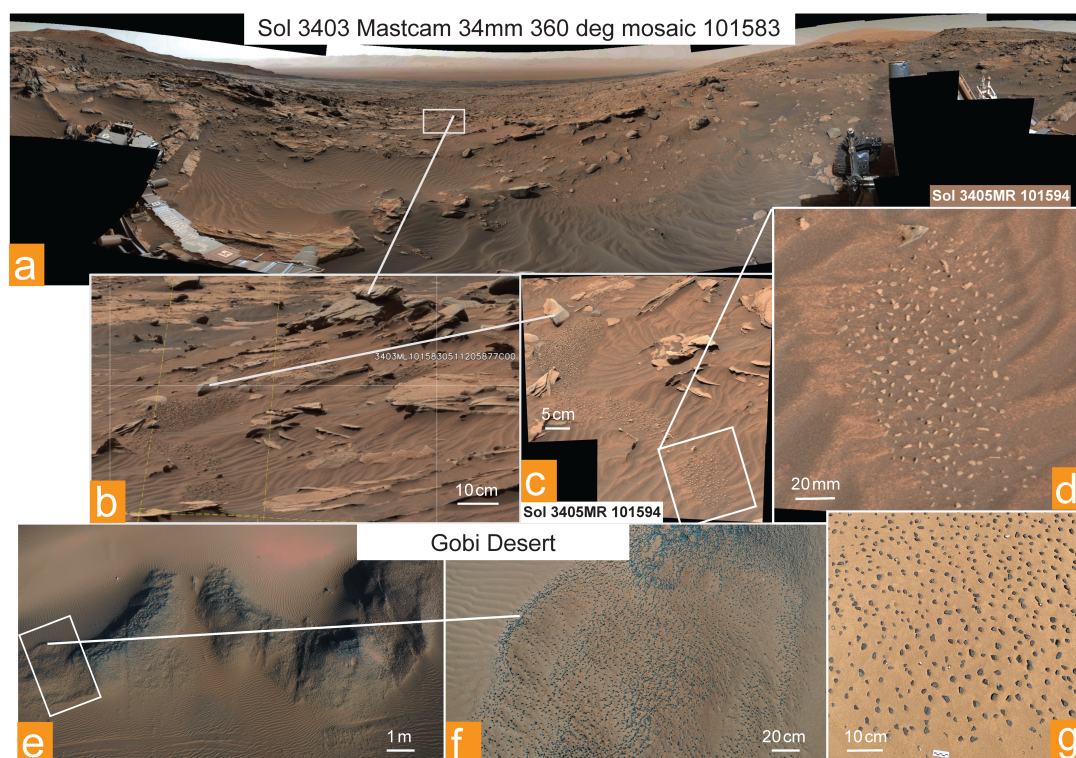


Fig. 1. Context for the patches of uniformly distributed pebble-sized clasts on aeolian sand on Mars and Earth. (a) Panorama of the Mars landscape in Gale Crater on Sol 3403. **(b)** Close up of the white rectangle area in image (a) (Sol 3403). **(c)** Enlargement of the region near the rock at ends of white line. Rectangle shows location of the **(d)** subframe. **(d)** Patch of pebbles showing distinct uniformity in spacing and size (Sol 3405). Image credits: NASA/JPL-Caltech/MSSS. **(e)** Drone (DJI Mavic 3T) overview of a study site in the Gobi desert, China, see Materials and Methods for details. The width of the field of view is approximately 30 m. **(f)** Close up of the white rectangle area in image (g). **(g)** Similar patch displaying distinct uniformity. The scale bar is 10 cm-long. Image credits: (e-g) Quan-Xing Liu.

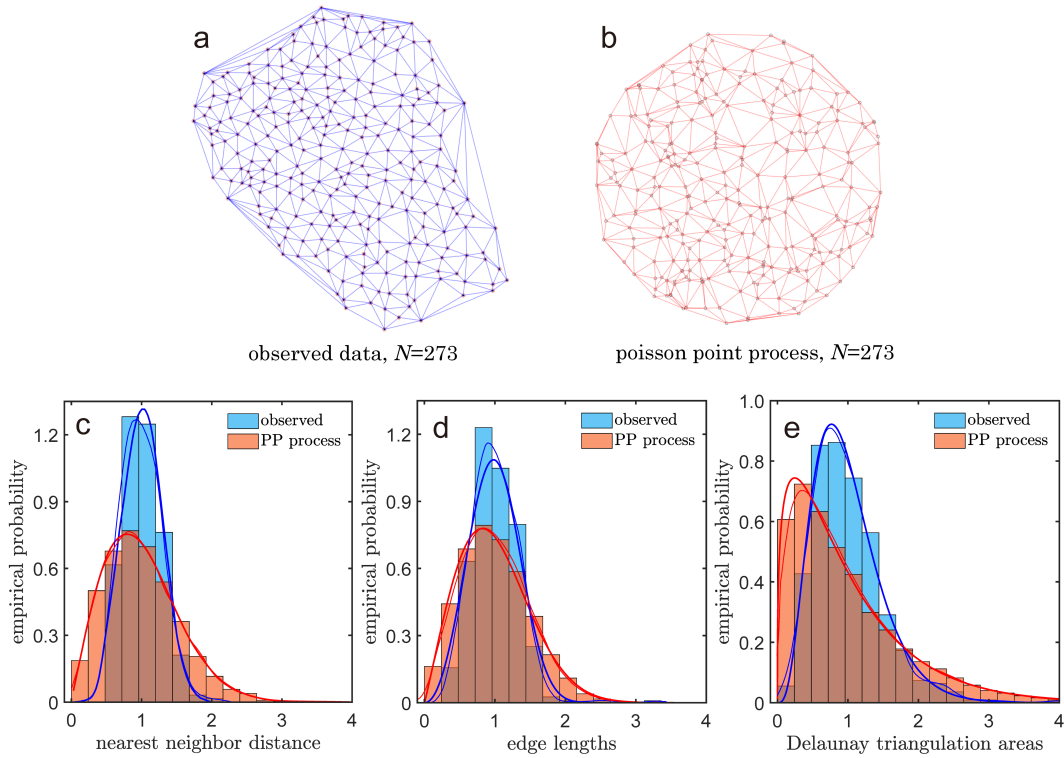


Fig. 2. Comparing observed clasts (blue in all insets) with random points generated by the Poisson process (orange in all insets). Delaunay triangulations (a) for the clasts imaged on sols 3403 and 3405, shown in Fig. 1d, and the random points (b) generated with $N = 273$ vertices. Normalized empirical distributions of nearest neighbor distance (c), edge length (d), and triangle area (e). The normalization is conducted using probability density function for a Gaussian distribution. Thin dashed and thick solid lines show the kernel estimators and the best-fit probability density functions (Weibull distribution for the nearest neighbor distance and edge length; Gamma distribution for the triangle area). Results for other sites are similar (Figs. S4 and S5).

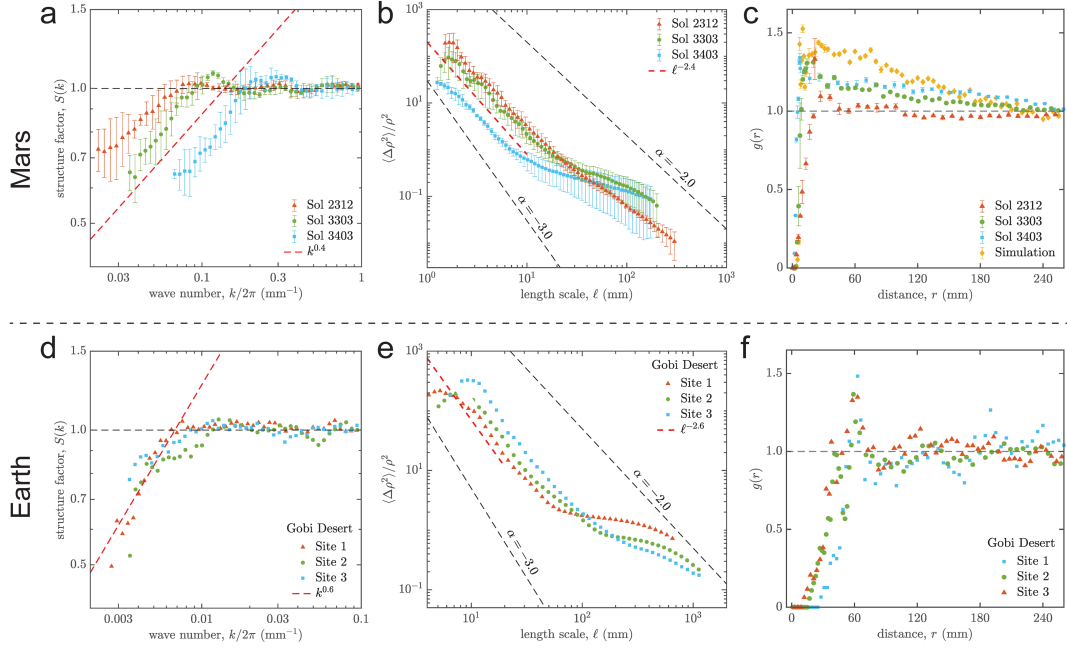


Fig. 3 Spatial distributions of clasts are characteristic of disordered hyperuniformity. (a) Structure factors for clasts in the study images in Mars' Gale Crater as a function of wave number for three sites imaged on different dates and locations along Curiosity's route: sol 2312 (orange, number $n = 4$ adjacent clasts areas, [Table S1](#)), sol 3303 (green, $n = 3$), and sol 3403 (blue, $n = 3$). Red dashed line represents the scaling law for a disordered hyperuniform distribution with exponent of 0.4 for $S(k)$. The red dashed line represents the $k^{0.4}$ trend; it corresponds to $\alpha = -2.4$ for density fluctuations. (b) Clast density fluctuations versus size of study window, which limits the maximal measurement scale. (c) Quantitative pair-correlation function $g(r)$ of clasts from simulation and observations. Note that all pair correlation functions decay slowly to unity as r increases, implying the existence of long-range correlations between clasts. (d to f) Correspond to Mars panels a through c for three sites on Earth in the Gobi Desert. All figures show characteristics of disordered hyperuniformity. All error bars denote one standard deviation, mean \pm SD.

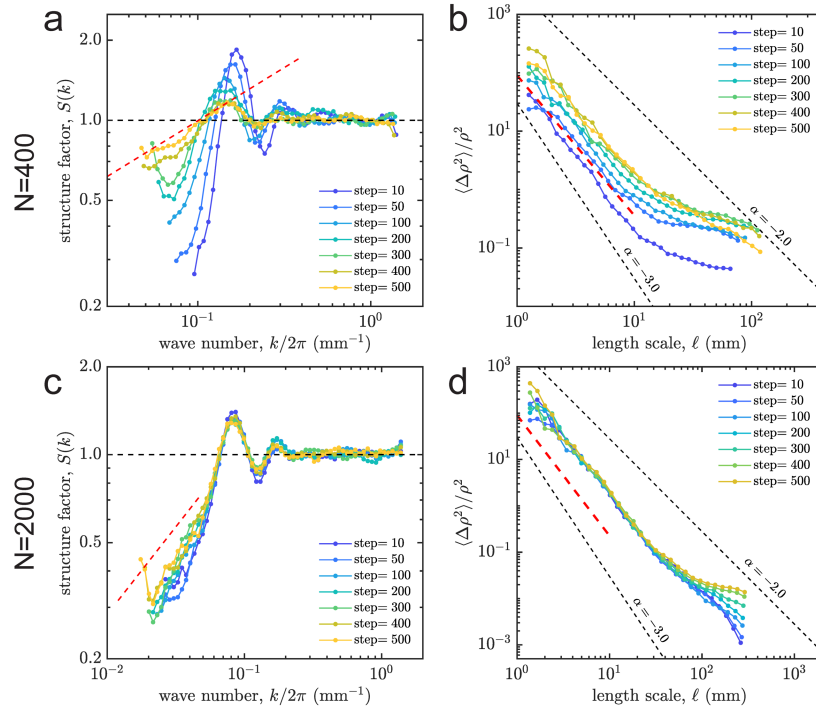


Fig. 4. Simulated spatial distributions of clasts. Simulations show the time evolution of structure factors and density fluctuations of clast distributions with different numbers of clasts, $N = 400$ and 2000 . The exponent of the static structure factor converges to 0.4 (red dashed line) with increasing time steps in (a), which corresponds to an exponent, α , close to -2.4 for the density fluctuations (red dashed line) in (b). The exponent of the static structure factor converges to 0.6 (red dashed line) in (c), which corresponds to $\alpha \sim -2.6$ (red dashed line, d). Simulation results are in good agreement with observed data; they all reflect local hyperuniformity within a range 5 to 10 times the clast radius.

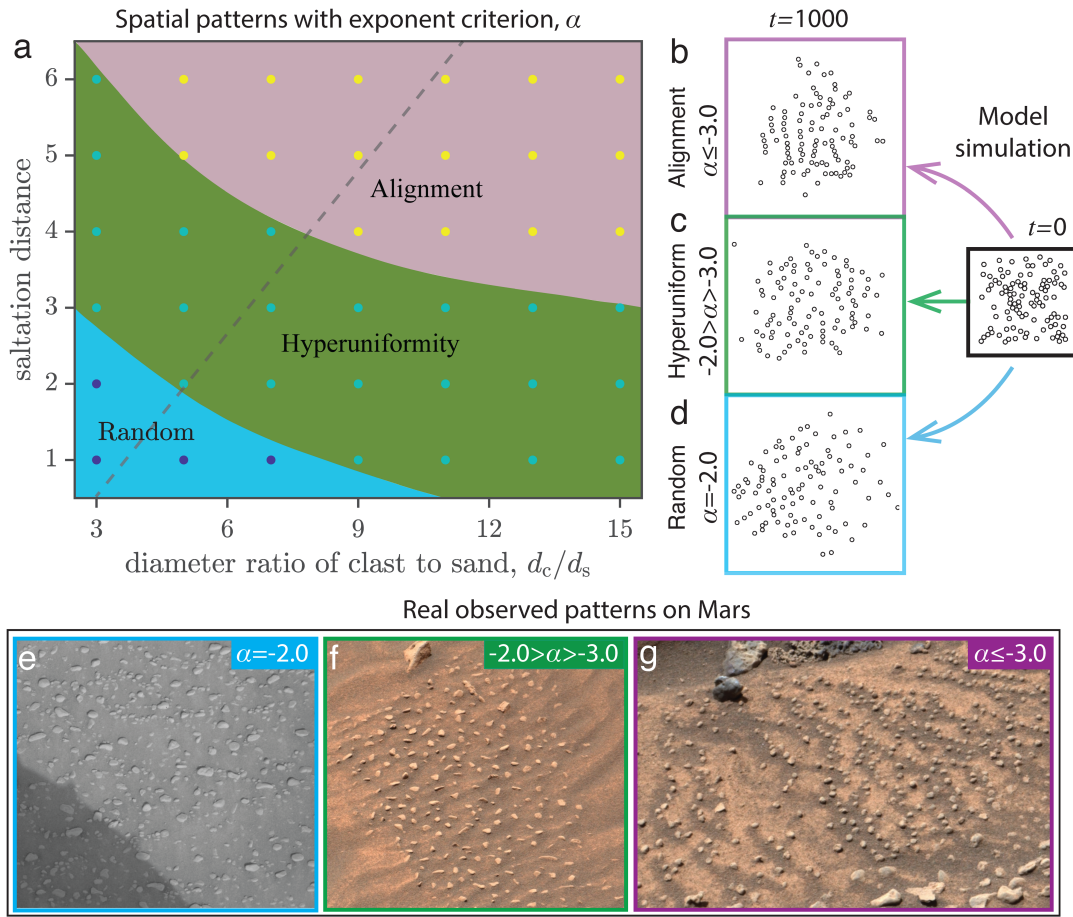


Fig. 5. Model-predicted regimes of clast spatial patterns controlled by saltation distance and diameter ratio of clast to sand. (a) Phase diagram for simulated clast distributions with $N = 400$ shown in Fig. 4. Saltation distance is an index of wind strength and sand transport. The circles are the simulation parameters and are identified by the exponent of hyperuniformity criterion based on 5 replications ($n = 5$) with same parameters and initial conditions. The gray dashed line represents the numerical simulation for panels b to d. (b-d) Examples of spatial distributions starting from the same initial spatial configuration corresponding to three different regimes, alignment (b), hyperuniform (c), and random distribution (d) at $t = 1000$. (e-g) Observed pebble distributions resembling the simulation results, random distributions (e, Sol 2320), hyperuniform distributions (f, Sol 3405), and alignments (g, Sol 3737). Image credits: (e to g) NASA/JPL-Caltech/MSSS.

Materials and Methods

Data collection.

The Mars Science Laboratory (MSL) rover images used in this work are archived for free public access by the NASA Planetary Data System (PDS). Within the PDS, MSL image data are available at <https://pds-imaging.jpl.nasa.gov/volumes/msl.html> (e.g., Mastcam data at <https://doi.org/10.17189/1520328>). The clasts images from Mars can also be downloaded from <https://mars.nasa.gov/msl/multimedia/raw-images/>. Image numbers and details are listed in [Tables S1](#) and [S2](#). The mosaic used in [Fig. 1](#) was produced by Malin Space Science Systems (MSSS) using MSL image data (images acquired by NASA/JPL-Caltech/MSSS). Note that although many MSL images include clasts along the Curiosity trajectory ([50](#)), many do not display extensive uniform clast domains, resulting in a limited total number of images. Only some of the orthophotos used here are included for precise analysis. The date of data acquisition is referenced as 'sol', denoting Martian days for the Curiosity rover.

The images of clast patches on Earth used in this work are from study sites in the Gobi desert in northwestern China, $38^{\circ}42'6''$ N, $105^{\circ}14'18''$ E (Alxa Left Banner, [Figs. 1e to G](#) and [Fig. S3](#)). The images depicting uniform clasts were collected at in the western region of the Gobi Desert, adjacent to the Tengger desert, where dispersed clasts on fine sand are common. We present one of the largest clast patches observed during our field investigation, using high-resolution images ([Fig. S3a](#) and [Fig. 1e](#)) taken with a DJI Mavic 3T drone from 20 meters above the ground with a resolution of about 0.4 cm per pixel. The mean slope of the area with ripples in this figure is $\sim 9^{\circ}$ with high precision RTK (Real-Time Kinematic) elevation.

Image analysis.

We first convert the color scenes to grayscale images, and extract the clast center points after binarizing, using MATLAB and Otsu's method ([56](#)), which chooses the threshold value to minimize the intraclass variance of the threshold black and white pixels. We, then 1) custom-made MATLAB program correct the positions where the density of clasts is high, because two close clasts might be processed as one due to shadows. Though we have adjusted the threshold for the binarization, several clasts still require custom-code correction. 2) determine density fluctuations from the data with different window sizes (sol 2312: $l = 12$ to 45 mm; sol 3303: $l = 8$ to 30 mm; sol 3403: $l = 4$ to 10 mm). All custom-made MATLAB programs used for position tracking have been adapted from existing literature focused on dense mussel beds ([7](#)).

Comparison of the data with distributions generated with the Poisson point process.

Let $f_o^{\text{emp}}(\cdot)$ and $f_s^{\text{emp}}(\cdot)$ denote the empirical probability density associated with the observed and simulated data (Poisson process) weighted by the sample mean. After removing the edges and triangles adjacent to the domain boundary, we computed the empirical distributions of the triangle *areas* (i.e., $f_o^{\text{emp}}(A)$ and $f_s^{\text{emp}}(A)$) and the edge *lengths* (i.e., $f_o^{\text{emp}}(L)$ and $f_s^{\text{emp}}(L)$). Our null hypothesis is that the two samples are drawn from a close-related continuous distribution. The two-sided Kolmogorov-Smirnov tests at the $\alpha = 5\%$ significance level yield $p = 1.02 \times 10^{-19}$ and 8.23×10^{-8} for the asymptotic probabilities for the area and the edge length distributions, respectively. As $p < 0.05$, we reject the null hypothesis for both the area and the edge length distributions and conclude that there is strong evidence that the distributions differ between those generated by Poisson process and the observed data.

To compare observed and simulated distributions further (Fig. 2, a and b), we use the kernel densities to obtain a smooth estimate of the discrete data on nearest neighbor distance, edge length, and area (Fig. 2, c to e). The area distributions $f_o^{\text{emp}}(A)$ and $f_s^{\text{emp}}(A)$ both follow Gamma distributions, whereas the edge lengths $f_o^{\text{emp}}(L)$ and $f_s^{\text{emp}}(L)$ are more consistent with Weibull distributions (thick solid lines). The best-fit parameters (denoted as a and b) of these two-parameter distributions (57) and their 95% level-confidence intervals are summarized in Table S3.

We note that the pairwise regions *spanned* by the confidence intervals of the parameters a and b are nonoverlapping for both the $f_o^{\text{emp}}(A)$, $f_s^{\text{emp}}(A)$ and the $f_o^{\text{emp}}(L)$ and $f_s^{\text{emp}}(L)$ pairs. This demonstrates geometrically that the recorded data indeed differ from a point dataset generated by a Poisson point process. We compare the triangulated meshes associated with both datasets and we find that the variances both of the triangle area and the triangle edge length are smaller in the investigated empirical dataset (Table S4 and Fig. 2). We recorded the same for all studied images, so we conclude that the uniformity in the studied images of clasts all surpass the uniformity of the Poisson point process (Tables S5 and S6, and Figs. S4 and S5), which is a strong indicator that the clast distributions are self-organized, rather than produced by chance.

Cellular model of clast displacements on a dynamic sand surface.

The model consists of two parts: the development of the surface of wind-erodible sand and clast displacements caused by the wind over that surface. To simulate the sand surface simply, we adapt a cellular model of eolian dune development similar to Werner's (22). Its basic elements are: 1) a square lattice with an initially uniform sand thickness (such as 15 sand grains) and horizontal surface; 2) randomly chosen units (a volume much larger than the grain size) of sand on the lattice are transported downwind a distance l ; and 3) at the new location, the sand unit is deposited with a probability p ($p < 1$ and if it is in a shadow zone protected from the direct impact of

saltating grains $p = 1$). The values of p and l effectively represent the local wind speed that controls the distance of sand transport and rates of deposition and erosion, higher values of l (longer saltation distance) and lower values of p (smaller deposition probability) lead to faster transport. Shadow zones are defined as areas not directly impacted by saltating grains; they would not receive direct light if the surface were illuminated by an upwind light source angled downward 15° from the horizontal. The down-wind length of shadow area is about $1/\tan 15^\circ \approx 4.0$ units. Moreover, if a sand unit is not deposited where it lands, it continues downwind a distance l until deposition occurs. Lastly, because of net deposition, the sand surface rises at the new location, and conversely it drops where there is a net divergence of sand. Due to the inferred lack of cohesion of the sand, the maximum surface slope is the angle of repose (i.e., assumed to be $\sim 30^\circ$). In this simulation, periodic boundary conditions are used in two-dimensions.

To study closely the evolution of clast distributions, we coupled the simulated dynamics of the ripples to the displacement of clasts on the surface much as was done in the published model (24) to study closely the evolution of clast distributions. Clasts resting on sand enhanced erosion on their windward side, so in these simulations, the deposition probability of the foreshadow zone of the clasts is zero and the shadow zones contain two parts, clasts and sand. In areas that belong to both shadow zones and foreshadow zones, according to the net depositional effect of obstacles (58), the shadow zone takes precedence; it is represented by $p = 1$. Clasts roll down slope when the local bed slope beneath the center of each clast exceeds a threshold value given by Ψ , $\frac{\partial h}{\partial x,y} \geq \tan \Psi$. They continue rolling downhill until the local slope decreases below this threshold. According to a previous study (59), the angle Ψ of repose or stability for a single clast is $\Psi = \alpha \left(\frac{D}{\bar{K}}\right)^{-\beta}$, D is the clast diameter, \bar{K} is the mean diameter of the substrate (sand grains). Assuming that $\beta \sim 0.3$, $\alpha \sim 40^\circ$ and D is ~ 7 times larger than sand grains, Ψ is about $40^\circ \times 7^{-0.3} \sim 22^\circ$, which corresponding to a max sand height difference about $\tan 22^\circ \times \frac{7}{2} (1 + \sin 22^\circ) \sim 2.0$ units.

In short, in the simulations the probability p of deposition exerts the primary control on the formation of ripples. The local surface steepening due to ripple migration and erosion on leading side of pebbles destabilizes them, causing some to tumble.

Pair correlation function.

Pair correlation functions $g_2(r)$ define the average number of particles surrounding a reference particle. It is a simple summary statistic that can be used to characterize a tendency toward aggregation (small distances r that $g_2(r) > 1$) or dispersion (60). It

is calculated as $g_2(r) = \frac{1}{N\rho} \langle \sum_i \sum_j \delta(\mathbf{r}_{ji} - r) \rangle$ and ($i \neq j$), where ρ is the number density of particles, N is the total number of particles, $\langle \rangle$ denotes the ensemble average, \mathbf{r}_{ji} is the distance between particle i and particle j . The position of the first peak denotes the average distance between the particles, or indicates that particles tend to be found at that distance from each other more frequently than at other distances.

Density fluctuation and hyperuniform distributions.

Density fluctuations describe how density variations at different points in space are related to each other. In two dimensions, density fluctuations are calculated as $\langle \Delta\rho^2 \rangle \equiv \langle \rho^2(\ell) \rangle - \langle \rho \rangle^2$ for square interrogation windows of different sizes ℓ , $\langle \rangle$ denotes the ensemble average and ρ is the average density of the system. $\langle \Delta\rho^2 \rangle \sim \ell^{-2}$ represents a random state. Importantly for this paper, systems whose fluctuations decay faster—or in other words, density fluctuations are suppressed, $\langle \Delta\rho^2 \rangle \sim \ell^\alpha$ with $-3 \leq \alpha < -2$, are called hyperuniform. The more uniform a system is, the larger α is. Systems resembling perfectly periodic arrays like crystals can achieve or closely approach the maximum value: $\alpha = -3$.

Structure factors.

Structure factors, $S(k)$, are useful to describe the distribution of particle density in systems over a range of wavelength, ℓ . They provide information about the spatial correlations (e.g. positions, ordering, and fluctuations) between particles in reciprocal space. It is calculated as:

$$S(k) = \frac{1}{N} \langle | \sum_{j=1}^N e^{-ik \cdot \mathbf{r}^{(j)}} |^2 \rangle,$$

where N is the total number of particles, \mathbf{r} is the particle position, \mathbf{k} is the wave number, $k = 2\pi/\ell$. In two dimensions, systems whose fluctuations decay faster, $S(k) \sim k^\lambda$, with $0 < \lambda \leq 1$ when $k \rightarrow 0$, are called hyperuniform. Additionally, perfectly periodic arrays like crystals can achieve or closely approach the maximum value of $\lambda = 1$.

The comparison of several different two-dimensional point configurations can be found in Ref. (30).